

Supplementary Information

Photothermal actuated origamis based on graphene oxide-cellulose programmable bilayers

Dace Gao, Meng-Fang Lin, Jiaqing Xiong, Shaohui Li, Shi Nee Lou, Yizhi Liu, Jing-Hao Ciou, Xinran Zhou and Pooi See Lee

Note S1. Tensile tests of GO and EC thin films

We performed tensile tests to acquire the Young's moduli of GO and EC thin films for theoretical calculation and FEA simulation. Specimens were prepared based on ASTM D638-14 standard method, where GO and EC thin films were cut into dumbbell shape (D638-14 Type V) as photographed in Figure S1. The width and length of the specimens' narrow section are 3.18 mm and 9.53 mm, respectively, while the gripping distance is 25.4 mm. The tests were conducted by a dynamic mechanical analyzer (DMA, MTS Criterion Model 42), and the thin-film dumbbells were loaded with in-plane uniaxial tension by a constant straining speed (2 mm/min) until fracture. Detailed mechanical properties derived from tensile tests are summarized in table S1, in which E is Young's modulus linearly fitted as the slope of the elastic regime, ϵ_y is the yield strain, ϵ and σ are the ultimate tensile strain and tensile strength at the fracture point.

A representative stress-strain curve of EC is plotted in Figure S2a, which exhibits an elastic regime with moderate slope and a long plastic regime. The average Young's modulus of EC is determined as 0.78 ± 0.05 GPa with a narrow value distribution, revealing our EC film's good homogeneity and uniform mechanical property. It can be regarded as a soft plastic since a modulus of 0.78 GPa is three folds smaller than that of polyethylene terephthalate (PET, 2.3 GPa) and polyimide (PI, 2.45 GPa), and is comparable with crosslinked polyethylene (PE, 0.5 GPa).¹ Besides, the existence of yield point (at $7.03 \pm 0.34\%$ yield strain) and the long ductile elongation regime (up to $70.19 \pm 6.43\%$ ultimate tensile strain) strongly indicates the amorphous nature of EC. The large under-curve area manifests

EC film's toughness considering the amount of energy it absorbed before breakage. In general, the softness of EC is beneficial to fast shape transformation, yet it is tough enough to ensure structural robustness in 3D architectures. The Young's modulus of GO is measured to be 1.54 ± 0.11 GPa with an average strength of 34.02 ± 1.79 MPa. These values are much lower than the parameters provided in previous reports where GO sheets were electrostatically crosslinked by metal cation byproducts from the synthesis,² but show similarity to GO films derived from sufficiently washed dispersion with ion species removed.³

Table S1. Summary of the tensile test results of multiple samples being tested

Sample No.	t (μm)	E (GPa)	ε_y (%)	ε (%)	σ (MPa)
EC-1	27	0.70	7.6	74.7	66
EC-2	25	0.74	6.5	75.6	65
EC-3	26	0.73	7.1	63.8	60
EC-4	23	0.75	7.3	59.5	66
EC-5	26	0.84	6.7	67.7	67
EC-6	27	0.82	6.9	72.5	68
EC-7	26	0.85	6.9	67.2	63
EC-8	25	0.84	7.3	80.5	76
GO-1	23	1.40	N/A	3.8	33
GO-2	22	1.61	N/A	3.9	35
GO-3	22	1.71	N/A	4.1	33
GO-4	23	1.51	N/A	4.1	32
GO-5	23	1.45	N/A	4.5	37

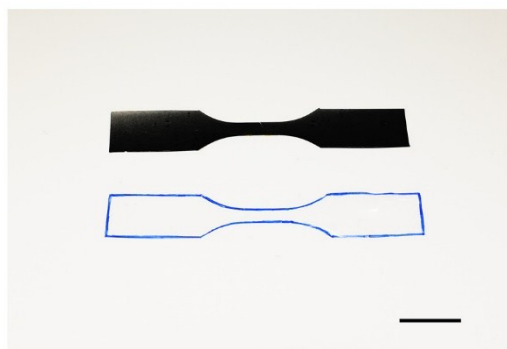


Fig. S1. Dumbbell shaped GO (black) and EC (transparent) thin films for DMA test. The edge of EC is colored to enhance visibility. Scale bar: 1 cm.

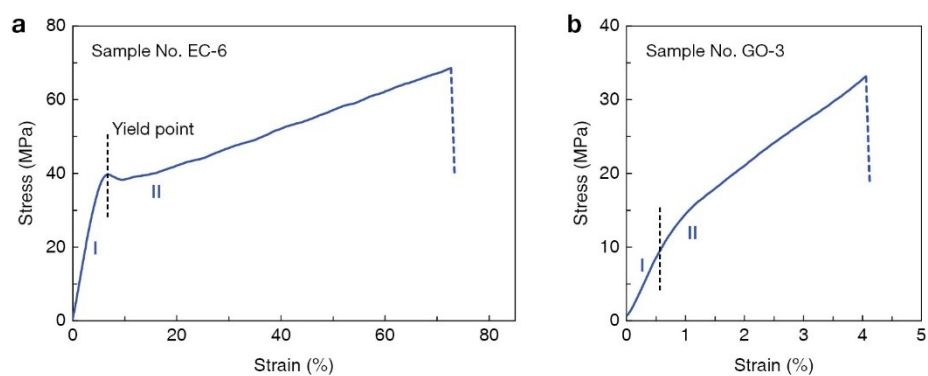


Fig. S2. Representative stress-strain curves of (a) EC and (b) GO thin films.

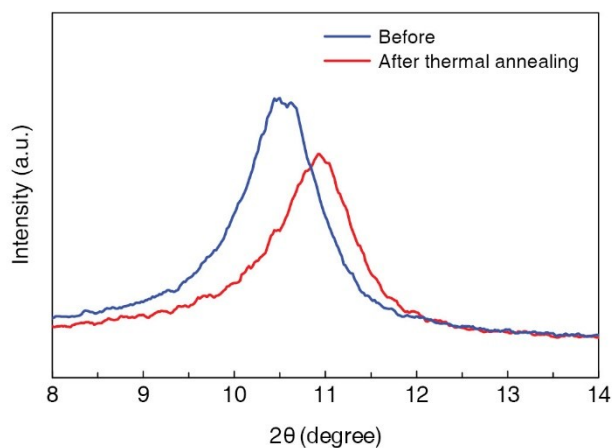


Fig. S3. XRD patterns depicting the hydrophilic region of GO before and after thermal annealing. Peak shift from 10.4° to 11.0° indicates the irreversible loss of “free water” and a more condensed GO package.

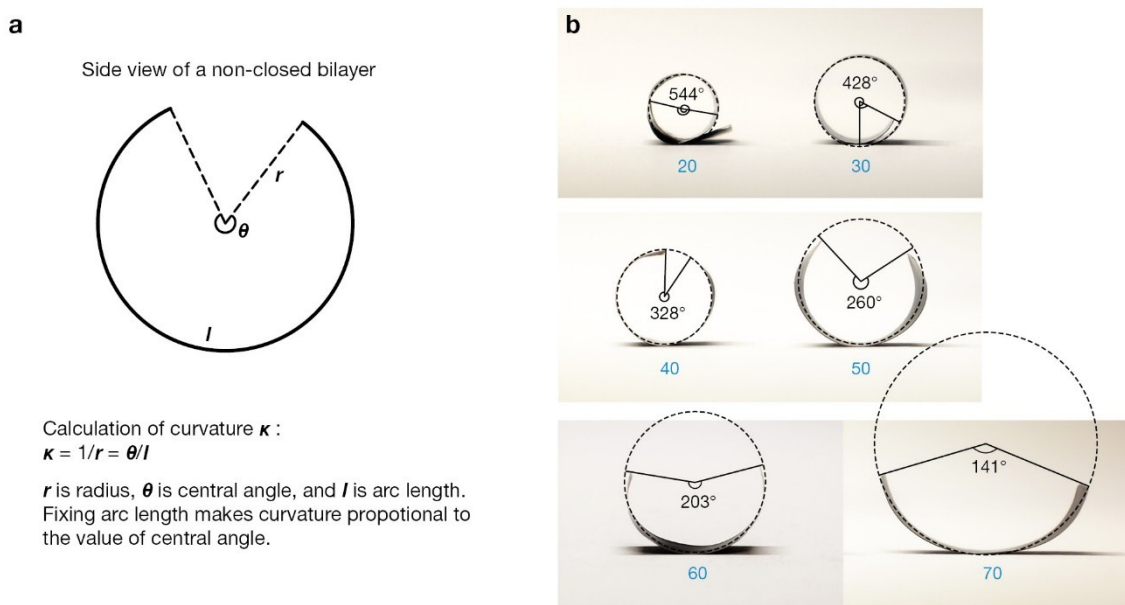


Fig. S4. (a) Schematic showing the curvature calculating method. (b) Central angle measurement of bimorphs with different EC thickness for curvature evaluation. EC thickness is labeled below each photo with unit in μm .

Note S2. Theoretical model of bimorph curvature

The following theoretical derivation is based on the bending theory in mechanics of materials. Timoshenko's investigation on bi-metal thermal bending problem is taken as reference.⁴ The calculation involves several prerequisite simplifications, including: (1) we adopt constant CTE of both materials within the considered temperature range to eliminate the complexity of non-linear problems; (2) we neglect the materials' expansion or contraction in width and thickness, despite that in real conditions thermal strain exist in all three coordinate directions. It is considered that the above assumptions only lead to acceptable deviation from actual situations, and the as deduced model is useful in predicting the curvatures of the GO-EC bimorphs.

A bilayer beam model is illustrated in Figure S5a. It consists of a top EC layer and a bottom GO layer which are tightly bonded without interfacial sliding. Here t_1 and t_2 are the thicknesses of EC and GO, respectively; the width (w) of the beam is normalized as unity. It is considered that the initial temperature T_0 is 90 °C (curing temperature), and a negative temperature gradient as $\Delta T = T - T_0 = -65$ °C leads to GO (with negative CTE α_2) expansion as well as EC (with positive CTE α_1) contraction. Thereafter the beam will bend in concave to reach mechanics equilibrium (Figure S5b). We examine the left-hand side of cross-section mn , which should remain planar and normal to the longitude axis during deformation according to the theorem of pure bending.⁵ On the cross section, the relative movement between the two layers induces a pair of mutual force: axial tensile force P_1 and compressive force P_2 , and two counterclockwise bending moments: M_1 on EC and M_2 on GO (Figure S5c).

There is no external force exerting on the beam, therefore the first consideration is the equilibrium of forces and moments:

$$P_1 = P_2 = P \#(1)$$

$$P \frac{t_1 + t_2}{2} = M_1 + M_2 \#(2)$$

Letting κ = curvature of the beam, and relating the moment-curvature relationship, we have

$$M_1 = E_1 I_1 \kappa \quad M_2 = E_2 I_2 \kappa$$

where E is the Young's modulus of each material and I is the moment of inertia of each layer's cross-sectional area. Substitute the above equations into (2)

$$P = \frac{2\kappa(E_1 I_1 + E_2 I_2)}{t_1 + t_2} \quad \#(3)$$

From the geometrical consideration, the elongations at the bearing interface of both layers are identical:

$$\alpha_1 \Delta T + \frac{P_1}{E_1 t_1} + \frac{t_1 \kappa}{2} = \alpha_2 \Delta T - \frac{P_2}{E_2 t_2} - \frac{t_2 \kappa}{2} \quad \#(4)$$

Integrating (3) and (4) we get

$$\kappa = \frac{(\alpha_2 - \alpha_1) \Delta T}{\frac{t_1 + t_2}{2} + \frac{2(E_1 I_1 + E_2 I_2)}{t_1 + t_2} \left(\frac{1}{E_1 I_1} + \frac{1}{E_2 I_2} \right)} \quad \#(5)$$

Letting

$$m = \frac{t_1}{t_2} \quad n = \frac{E_1}{E_2}$$

and replacing

$$I_1 = \frac{t_1^3}{12} \quad I_2 = \frac{t_2^3}{12} \quad \lambda = \frac{(\alpha_2 - \alpha_1) \Delta T}{t_2}$$

we finally obtain the equation describing the curvature dependence of layer thickness:

$$\kappa = \lambda \frac{6(m+1)}{3(m+1)^2 + (m^3 n + 1) \left(\frac{1}{mn} + 1 \right)} \quad \#(6)$$

When the bilayer is brought back to ambient environment ($T \approx 25$ °C, RH \approx 70%) after curing ($T_0 = 90$ °C), the modeling equation can reasonably predict the measured curvatures with a fitting coefficient of $\lambda = 11.2$ as shown in Fig 1f. As the thickness of GO (t_2) and environmental conditions are fixed, κ becomes a function of m , or the thickness of EC (t_1) as illustrated in Fig. S6.

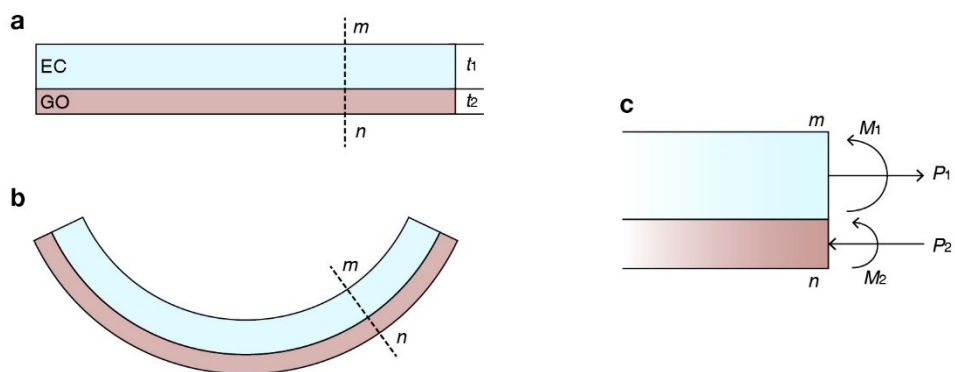


Fig. S5. Illustrations of the bilayer beam model in (a) unstrained and (b) strained conditions. (c) Force and moment analysis across an arbitrary cross section of the beam.

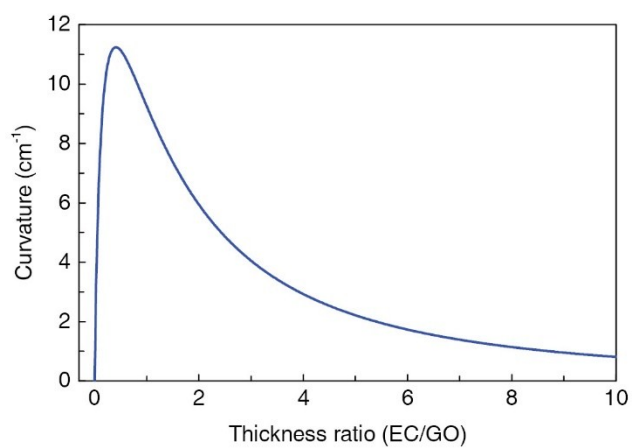


Fig. S6. The predicted curvature as a function of the thickness ratio of EC/GO under ambient environment.

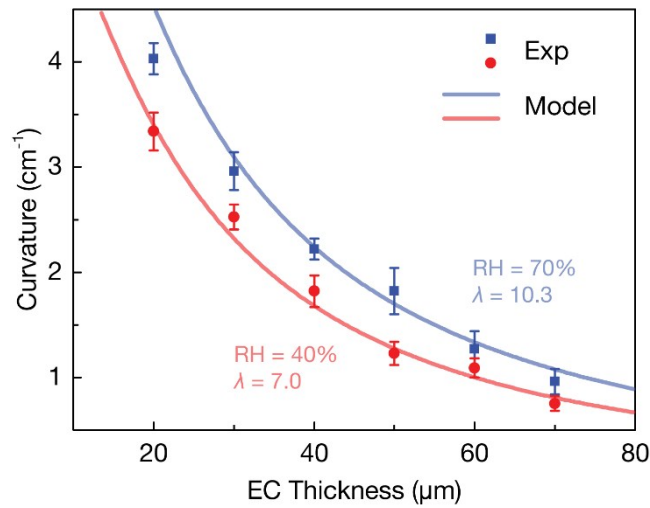


Fig. S7. Apart from temperature gradient and layer thicknesses, humidity level of the environment also influences the curvature generating process by manipulating the CTE mismatch between GO and EC ($\alpha_2 - \alpha_1$). We placed the bimorphs with different EC thickness in a climate chamber to precisely control the environmental conditions including temperature (fixed at 20 °C) and RH (controlled to be either 70% or 40%). Experimental results indicate that the bimorph curvatures get smaller when the environment is less humid. The modeling equation as derived in Note S2 can fit both data sets by adopting $\lambda = 10.3$ and $\lambda = 7.0$ under 70% and 40% RH, respectively, since a lower RH will result in a diminished CTE mismatch, leading to a smaller fitting coefficient λ .

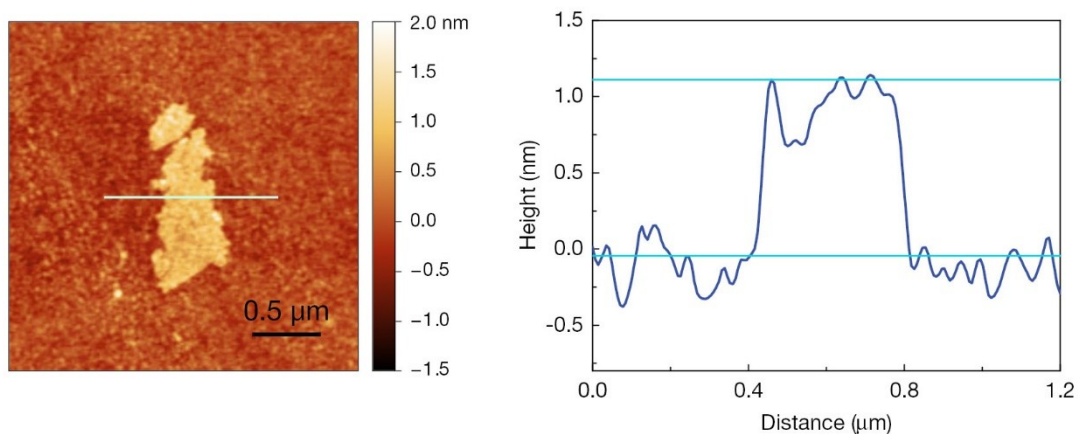


Fig. S8. AFM topographic-image and height profile of a monolayer GO.

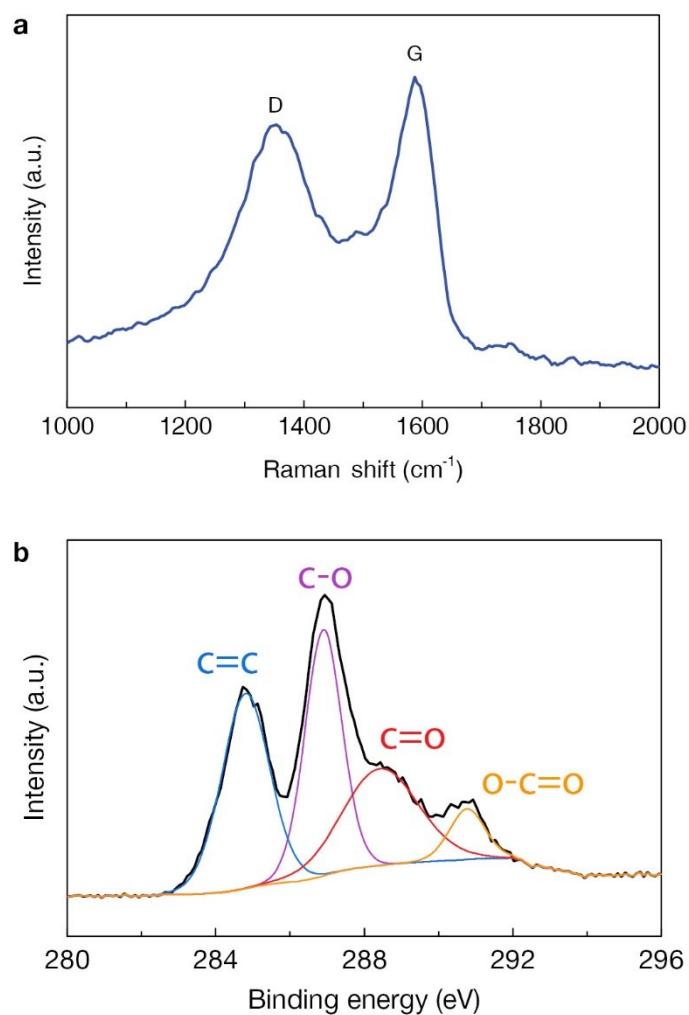


Fig. S9. (a) Raman spectrum of GO, in which G band represents in-phase vibration of sp^2 -carbon lattice, while D band represents crystalline disorder introduced by oxygen-containing groups. (b) XPS C 1s spectrum of GO. The spectrum can be deconvoluted into four major components: graphitic sp^2 carbon (C=C, 284.8 eV), oxidized sp^3 carbon in the form of epoxy/hydroxyl (C-O) 286.9 eV, carbonyl (C=O, 288.4 eV) and carboxylate (O-C=O, 290.8 eV). The XPS result indicates that the GO used in this work contains 66% oxidized carbon and 34% graphitic carbon, leading to a low sp^2/sp^3 ratio of 0.52.

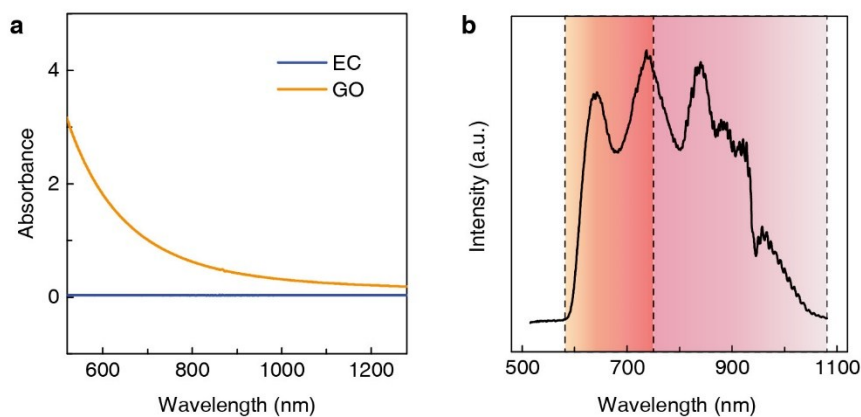


Fig. S10. (a) Light absorbance of GO and EC. The thickness of GO and EC films are 10 μm and 30 μm , respectively. (b) Emission spectrum of the light source (Philips BR125). It consists of visible red light (580nm - 750 nm) and NIR light (750 nm - 1080 nm).

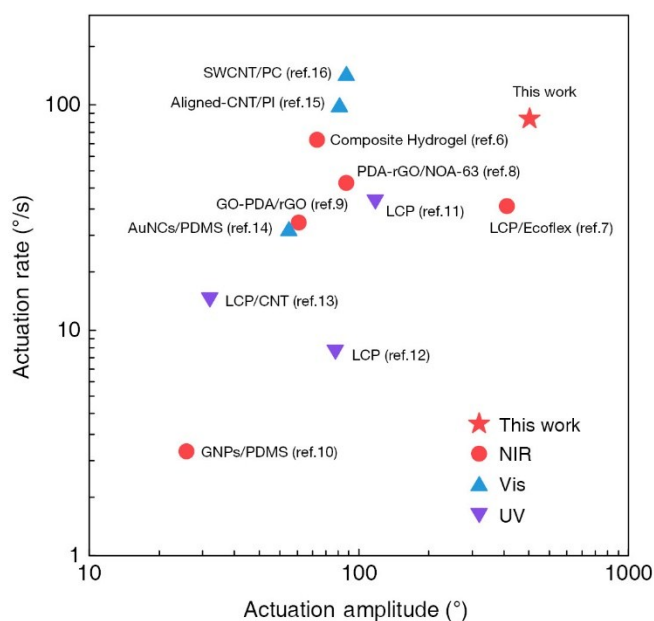


Fig. S11. Ashby plot comparing actuation amplitude and rate of various actuators driven by NIR,⁶⁻¹⁰ UV¹¹⁻¹³ and visible¹⁴⁻¹⁶ light, wherein LCP = liquid crystal polymer, PDA = polydopamine, rGO = reduced graphene oxide, CNT = carbon nanotube, AuNC = gold nanocrystal, GNP = graphene nanoplatelet, PC = polycarbonate, PI = polyimide.

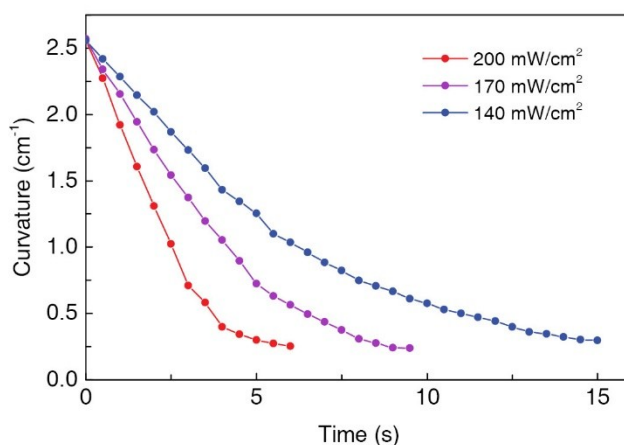


Fig. S12. Dynamic curvature changes of the bimorph PTA under different NIR intensity.

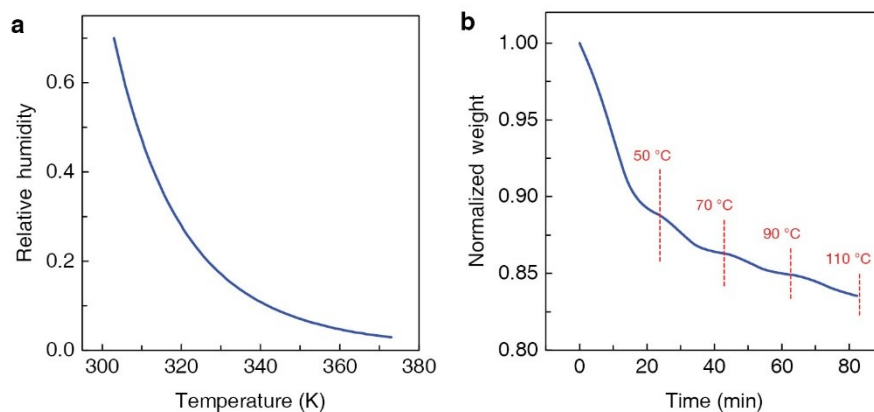


Fig. S13. (a) RH change with temperature. RH is defined as water partial pressure divided by its saturated vapor pressure. Water partial pressure is assumed as a constant which does not change with temperature, and the value is calculated to be c.a. 2916 Pa based on data provided by Singapore Meteorological Service Website. Saturated pressure is calculated based on Antoine equation with parameters referring to NIST Chemistry WebBook: $A = 5.2$, $B = 1733.9$, $C = -39.5$. (b) Water loss in GO measured by TGA. The heating program was set as 10 minutes heating followed by 10 minutes stabilization at each monitored temperature.

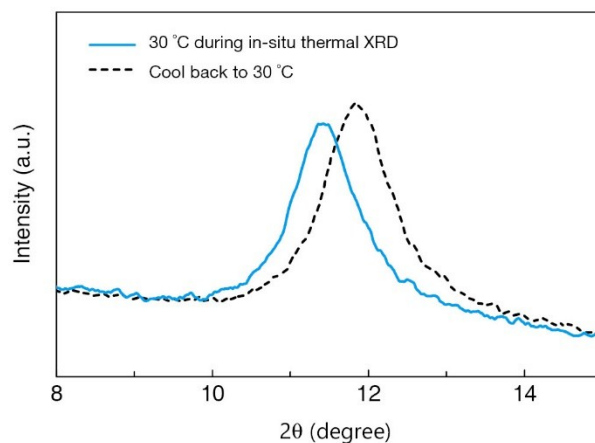


Fig. S14. XRD patterns confirming the reversibility of water desorption and adsorption. The slight mismatch between two peaks may attribute to further loss in “free water” during the long term and high temperature in-situ XRD process.

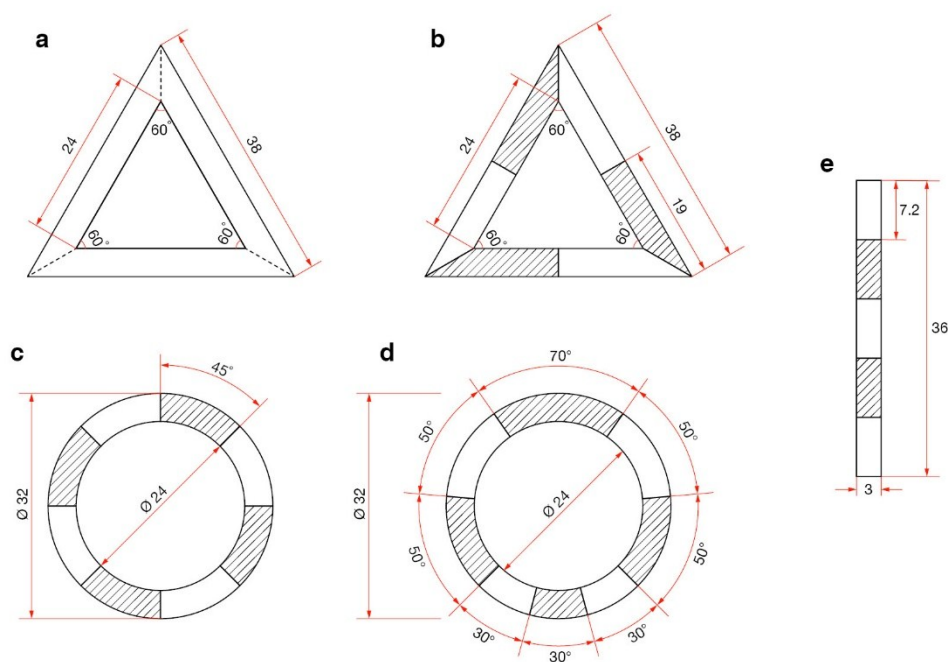


Fig. S15. Dimensional specification of the 2D layouts in Figure 4a1, 4b1, 4c1, 4d1 and 4h1.

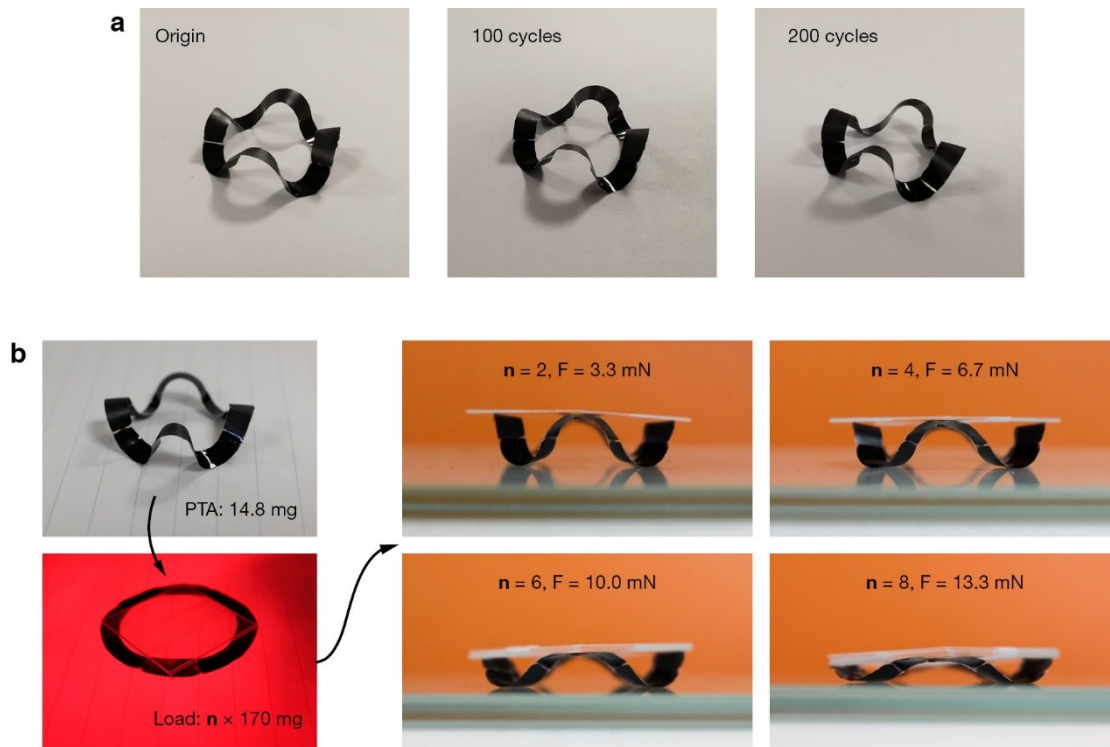


Fig. S16. (a) Photographs of a centrosymmetric annulus PTA as fabricated and after multiple actuation cycles. (b) Actuation of the centrosymmetric annulus PTA in the presence of normal loads tens of times larger than its own weight. The PTA weighs merely 14.8 mg, while the loads are multiples of 170 mg (weight of an individual piece of cover glass). The 3D PTA was initially flattened by NIR to load glass sheets on top, then allowed to buckle under a series of resisting weights until stabilized at the maximum lifting distances. Sideview photographs were taken for stroke evaluation and specific work calculation.

Table S2. Summary of representative stimuli-responsive 3D architectures based on diverse mechanisms

Active material	Stimulus	Mechanism	Performance	Ref.
Shape memory alloy	Resistive heating	Phase change	6 mm stroke, 0.3 N maximum force	17
Graphene/PNIPAM ^{a)}	Temperature	Polymer brush's Conformation change	51% strain, $\Delta T = 50\text{ }^{\circ}\text{C}$	18
Graphene/glass	Temperature	CTE mismatch	50% curvature change, $\Delta T = 100\text{ }^{\circ}\text{C}$	19
Liquid crystal elastomer	Temperature	Phase change	~ 3mm vertical stroke, $\Delta T = 150\text{ }^{\circ}\text{C}$	20
CNT-hydrogel composite	NIR light	Mass transport of water	90° bending, $\Delta T = 25\text{ }^{\circ}\text{C}$	21
GO/EC bilayer	NIR light	CTE mismatch	> 400° bending, $\Delta T = 25\text{ }^{\circ}\text{C}$	This work
Commercial plastic films	Fluid (gas/liquid)	Pressure differential	90% contraction, - 70 kPa pressure	22
Dielectric elastomer	High voltage	Electrostatic force	25° bending under 6 kV	23

a) PNIPAM = poly(N-isopropylacrylamide)

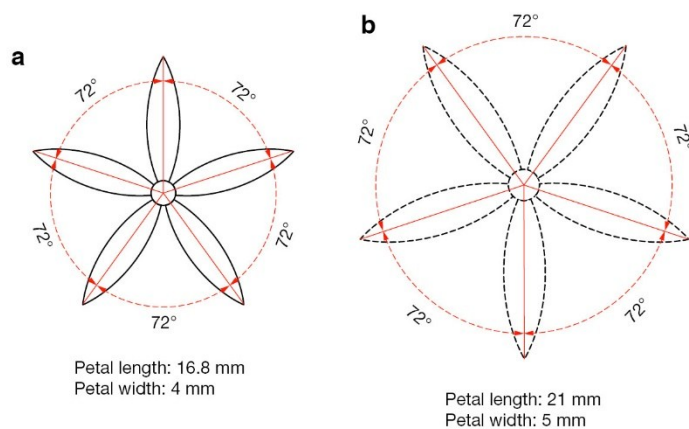


Fig. S17. Dimensional specification of the 3D-PTA flower.

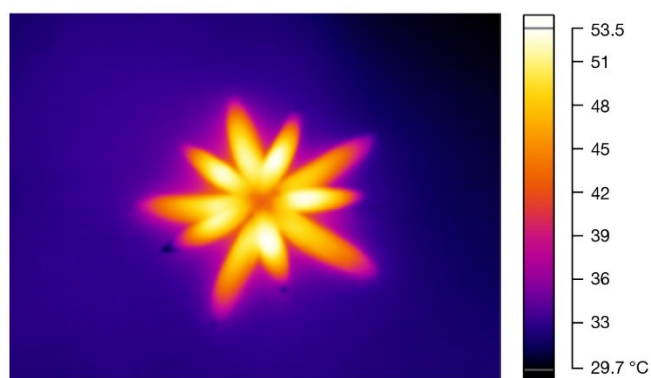


Fig. S18. Thermogram of the 3D-PTA flower under 140 mW/cm^2 NIR irradiation. Average temperature of outer petals is relatively lower due to their direct contact with substrate and faster heat dissipation.

References

1. T. R. Crompton, *Physical testing of plastics*, Smithers Rapra, 2012.
2. D. A. Dikin, S. Stankovich, E. J. Zimmey, R. D. Piner, G. H. Dommett, G. Evmenenko, S. T. Nguyen and R. S. Ruoff, *Nature*, 2007, **448**, 457-460.
3. C. Luo, C. N. Yeh, J. M. L. Baltazar, C. L. Tsai and J. Huang, *Adv. Mater.*, 2018, **30**, 1706229.
4. S. Timoshenko, *J. Opt. Soc. Am. Rev. Sci. Instrum.*, 1925, **11**, 233-255.
5. J. M. Gere and B. J. Goodno, *Mechanics of Materials 5th*, Brooks Cole, 2001.
6. E. Wang, M. S. Desai and S. W. Lee, *Nano Lett.*, 2013, **13**, 2826-2830.
7. R. R. Kohlmeier and J. Chen, *Angew. Chem. Int. Ed. Engl.*, 2013, **52**, 9234-9237.
8. M. Ji, N. Jiang, J. Chang and J. Sun, *Adv. Funct. Mater.*, 2014, **24**, 5412-5419.
9. J. Mu, C. Hou, H. Wang, Y. Li, Q. Zhang and M. Zhu, *Sci. Adv.*, 2015, **1**, 1500533.
10. W. Jiang, D. Niu, H. Liu, C. Wang, T. Zhao, L. Yin, Y. Shi, B. Chen, Y. Ding and B. Lu, *Adv. Funct. Mater.*, 2014, **24**, 7598-7604.
11. T. Yoshino, M. Kondo, J. Mamiya, M. Kinoshita, Y. Yu and T. Ikeda, *Adv. Mater.*, 2010, **22**, 1361-1363.
12. C. L. van Oosten, C. W. Bastiaansen and D. J. Broer, *Nat. Mater.*, 2009, **8**, 677-682.
13. X. Sun, W. Wang, L. Qiu, W. Guo, Y. Yu and H. Peng, *Angew. Chem. Int. Ed. Engl.*, 2012, **51**, 8520-8524.
14. T. Lan, Y. Hu, G. Wu, X. Tao and W. Chen, *J. Mater. Chem. C*, 2015, **3**, 1888-1892.
15. J. Deng, J. Li, P. Chen, X. Fang, X. Sun, Y. Jiang, W. Weng, B. Wang and H. Peng, *J. Am. Chem. Soc.*, 2016, **138**, 225-230.
16. X. Zhang, Z. Yu, C. Wang, D. Zarrouk, J. W. Seo, J. C. Cheng, A. D. Buchan, K. Takei, Y. Zhao, J. W. Ager, J. Zhang, M. Hettick, M. C. Hersam, A. P. Pisano, R. S. Fearing and A. Javey, *Nat. Commun.*, 2014, **5**, 2983.
17. M. Boyvat, J. S. Koh and R. J. Wood, *Science Robotics*, 2017, **2**, eaan1544.
18. W. Xu, Z. Qin, C. T. Chen, H. R. Kwag, Q. Ma, A. Sarkar, M. J. Buehler and D. H. Gracias, *Sci. Adv.*, 2017, **3**, 1701084.
19. M. Z. Miskin, K. J. Dorsey, B. Bircan, Y. Han, D. A. Muller, P. L. McEuen and I. Cohen, *Proc. Natl. Acad. Sci. U. S. A.*, 2018, **115**, 466-470.
20. T. H. Ware, M. E. McConney, J. J. Wie, V. P. Tondiglia and T. J. White, *Science*, 2015, **347**, 982-984.
21. X. Zhang, C. L. Pint, M. H. Lee, B. E. Schubert, A. Jamshidi, K. Takei, H. Ko, A. Gillies, R. Bardhan, J. J. Urban, M. Wu, R. Fearing and A. Javey, *Nano Lett.*, 2011, **11**, 3239-3244.

22. S. Li, D. M. Vogt, D. Rus and R. J. Wood, *Proc. Natl. Acad. Sci. U. S. A.*, 2017, **114**, 13132-13137.
23. J. Wang, S. Li, D. Gao, J. Xiong and P. S. Lee, *NPG Asia Mater.*, 2019, **11**, 71.